Collisional excitation of doubly and triply deuterated ammonia ND2H and ND3 by H2

F. Daniel, C. Rist, A. Faure, E. Roueff, M. Gérin, D. C. Lis, P. Hily-Blant, A. Bacmann, L. Wiesenfeld

Monthly Notices
of the
ROYAL ASTRONOMICAL SOCIETY

MNRAS **457,** 1535–1549 (2016) doi:10.1093/mnras/stw084

Collisional excitation of doubly and triply deuterated ammonia ND_2H and ND_3 by H_2

F. Daniel,[1⋆] C. Rist,[1] A. Faure,[1⋆] E. Roueff,[2] M. Gérin,[3] D. C. Lis,[4,5] P. Hily-Blant,[1] A. Bacmann[1] and L. Wiesenfeld[1]

[1]*IPAG, Observatoire de Grenoble, Université Joseph Fourier, CNRS UMR5571, B.P. 53, F-38041 Grenoble Cedex 09, France*
[2]*LERMA, Observatoire de Paris, PSL Research University, CNRS, Sorbonne Universités, UPMC Univ. Paris 06, F-92190, Meudon, France*
[3]*LERMA, Observatoire de Paris, PSL Research University, CNRS, Sorbonne Universités, UPMC Univ. Paris 06, Ecole normale supérieure, F-75005 Paris, France*
[4]*LERMA, Observatoire de Paris, PSL Research University, CNRS, Sorbonne Universités, UPMC Univ. Paris 06, F-75014 Paris, France*
[5]*California Institute of Technology, Cahill Center for Astronomy and Astrophysics 301-17, Pasadena, CA 91125, USA*

Accepted 2016 January 8. Received 2016 January 6; in original form 2015 December 14

ABSTRACT

The availability of collisional rate coefficients is a prerequisite for an accurate interpretation of astrophysical observations, since the observed media often harbour densities where molecules are populated under non-local thermodynamic equilibrium conditions. In the current study, we present calculations of rate coefficients suitable to describe the various spin isomers of multiply deuterated ammonia, namely the ND_2H and ND_3 isotopologues. These calculations are based on the most accurate NH_3–H_2 potential energy surface available, which has been modified to describe the geometrical changes induced by the nuclear substitutions. The dynamical calculations are performed within the close-coupling formalism and are carried out in order to provide rate coefficients up to a temperature of $T = 50$ K. For the various isotopologues/symmetries, we provide rate coefficients for the energy levels below $\sim$100 cm^{-1}. Subsequently, these new rate coefficients are used in astrophysical models aimed at reproducing the NH_2D, ND_2H and ND_3 observations previously reported towards the pre-stellar cores B1b and 16293E. We thus update the estimates of the corresponding column densities and find a reasonable agreement with the previous models. In particular, the ortho-to-para ratios of NH_2D and NHD_2 are found to be consistent with the statistical ratios.

Key words: molecular data – molecular processes – scattering.

1 INTRODUCTION

Ammonia is an ubiquitous molecule in space, which has been observed in a large variety of media. In some of these places, the temperature can fall to a few kelvins, as in low-mass star-forming regions. Others, as for example shocked media, have temperatures as high as a few thousand kelvins. Depending on the temperature, the chemistry that leads to ammonia formation can follow different paths. Given the importance of this molecule, in particular in the context of nitrogen chemistry, much effort has been made in the past in order to characterize the corresponding formation or destruction mechanisms. This proved to be successful and nowadays, most of the observations can be, at least qualitatively, understood. In some cases, however, astrochemical models and observations still show discrepancies, as in the case of circumstellar envelopes where the models underpredict the observed molecular abundances by a few orders of magnitude (Menten et al. 2010). Additionally, in recent years, it was found that the nuclear–spin states of a given molecule are not necessarily populated according to simple statistical considerations. This is the case for ammonia, for which some observations report ortho-to-para ratios (OPR) in the range 0.5–0.7 (Hermsen et al. 1988; Persson et al. 2012), while a statistical ratio of 1 was expected in the past, for a formation in the gas phase. If ammonia is formed in the solid phase, and subsequently released from the grains, this ratio would be $\sim$2. Recently, astrochemical gas-phase models have been updated by including rigorous nuclear–spin selection rules relevant to describe the ammonia formation. It was found that ratios lower than 1 can be well accounted for by such models in the low temperature regime, where the H_2 gas is para enriched (Faure et al. 2013; Rist et al. 2013; Sipilä, Caselli & Harju 2015).

While NH_3 is observed in media that span a wide range of physical conditions, the detection of its multideuterated counterparts, i.e. ND_2H and ND_3, is restricted to cold regions. The reasons behind

⋆ E-mail: fabien.daniel@obs.ujf-grenoble.fr (FD); alexandre.faure@obs.ujf-grenoble.fr (AF)

this are now well established and lie in the fact that the deuterium enrichment comes from the difference of zero-point energies associated with the hydrogenated or deuterated isotopologues. These differences create a dichotomy in the chemical network. Indeed, the reactions that lead to deuterated species have, in general, exothermicities which are enhanced by comparison to the equivalent reactions that involve their hydrogenated counterparts. This effect creates a significant deuterium enrichment at low temperatures if H_2 is mainly in its para form. Indeed, in the high-temperature regime, the dichotomy between deuterated and hydrogenated molecules vanishes, since the difference of exothermicities become negligible with respect to the kinetic temperature. In the particular case of ammonia, the main formation route consists of a sequence of reactions involving H_2, which is initiated by the $N^+ + H_2 \rightarrow NH^+ + H$ reaction and ends with the dissociative recombination reaction $NH_4^+ + e^- \rightarrow NH_3 + H$ (see e.g. Dislaire et al. 2012). The initiating reaction has a small endothermicity (in the range 100–300 K; see e.g. Gerlich 1993). On the other hand, the endothermicity of the equivalent reaction involving HD and leading to ND^+ is reduced (20–70 K; see Marquette, Rebrion & Rowe 1988; Sunderlin & Armentrout 1994), which hence favours the deuteration processes at low temperatures. Finally, the abundances of the NH_3 isotopologues decrease with the number of deuterium atoms. Given the physical conditions characteristics of low-mass star-forming regions, which harbour low gas temperatures ($T \lesssim 20$ K) and relatively low gas densities ($n(H_2) \lesssim 10^7$ cm^{-3}), the low abundance implies that the signal associated with these isotopologues is weak, which makes the ND_2H and ND_3 molecules hard to detect with the current facilities. Hence, so far, the detection of all four deuterated isotopologues of ammonia is restricted to two astrophysical objects, the pre-stellar cores 16293E[1] and Barnard 1 (Roueff et al. 2005). This census has still to be enlarged to other objects to ensure statistically meaningful conclusions, starting with objects where ND_3 has already been observed, as in NGC 1333 (van der Tak et al. 2002).

This work is aimed at providing collisional rate coefficients for the ND_2H and ND_3 molecules, with p–H_2 as a collisional partner. For these molecules, earlier calculations were performed with He or H_2 with a reduced basis set (Machin 2006; Machin & Roueff 2007; Yang & Stancil 2008; Wiesenfeld et al. 2011). Such rate coefficients are essential in order to interpret the emission observed in astrophysical objects and imply solving a problem of quantum dynamics. Recently, similar calculations (Ma et al. 2015; Tkáč et al. 2015) were performed independently for NH_3 and ND_3 and using the potential energy surface (PES) reported by Maret et al. (2009), which is also used in this work. However, rather than providing collisional rate coefficients, the focus of Ma et al. (2015) or Tkáč et al. (2015) was to assess the possibility of testing the accuracy of the PES by comparing theoretical predictions based on the PES with experimental data. The comparisons performed so far show good agreement between experiments and theory at collision energies above 430 cm^{-1} (Tkáč et al. 2015).

This paper is organized as follows. The PES is described in Section 2 and the collisional dynamics based on this surface in Section 3. We then describe the rate coefficients in Section 4. In Section 5, we discuss the current results with respect to other related collisional systems. In Section 6, we use our new rate coefficients in order to re-interpret the observations previously reported towards 16293E and Barnard 1. Finally, we present our conclusions in Section 7.

[1] This pre-stellar core is sometimes referred as L1689N in the literature.

2 POTENTIAL ENERGY SURFACE

The collisional excitation of an isotopic homologue takes place on the same Born–Oppenheimer PES as the main isotopologue. All differences are therefore contained in the dynamical treatment. Within the rigid-rotor approximation, these differences involve changes in (i) the internal state-averaged geometry, (ii) the centre of mass position, (iii) the reduced mass of the total system, (iv) the energy level spacing and (v) the rotation of the principal axes of inertia. All these effects were considered here for ND_2H and ND_3, except the change of internal geometry: the averaged geometry of NH_3 was employed for both deuterated isotopologues, thereby neglecting the deuterium substitution effect on the N–H bond length and $\widehat{HNH}$ angle. This assumption was previously adopted for the NH_2D–H_2 and ND_2H–H_2 systems by Daniel et al. (2014) and Wiesenfeld et al. (2011), respectively. The (rigid-rotor) PES for ND_3–H_2 was thus again derived from the CCSD(T) NH_3–H_2 PES computed by Maret et al. (2009), but in the principal inertia axes of the isotopologue. We note that internal geometry effects in the estimate of the rate coefficients are expected to be only moderate ($\lesssim$ 20–30 per cent) at the temperatures investigated here, i.e. $T < 50$ K, as demonstrated by Scribano, Faure & Wiesenfeld (2010) for the D_2O–H_2 system.

The transformation between the reference frame of an isotopologue and the original frame of the NH_3–H_2 system can be found in Wiesenfeld et al. (2011, equations 2–3) where the γ angle is zero for ND_3 and the coordinates of the ND_3 centre of mass in the NH_3–H_2 reference frame are X_{CM}=0.0 bohr and Z_{CM}=−0.088548436 bohr (where X_{CM} and Z_{CM} were calculated for the average geometry of NH_3 used by Maret et al. 2009). As for NH_2D–H_2 and ND_2H–H_2, the ND_3–H_2 PES was generated on a grid of 87 000 points consisting of 3000 random angular configurations combined with 29 intermolecular distances in the range 3–15 bohr. This PES was expanded in products of spherical harmonics and rotation matrices (see equation 4 in Wiesenfeld et al. 2011), using a linear least-squares fit procedure detailed in Rist & Faure (2011). The fit actually employs the 120 terms expansion optimized for NH_3–H_2 by Maret et al. (2009), where details can be found. The final expansion thus includes anisotropies up to l_1=11 for ND_3 and l_2=4 for H_2. The root mean square residual was found to be lower than 1 cm^{-1} for intermonomer separations R larger than 4.5 bohr, with a corresponding mean error on the expansion coefficients smaller than 1 cm^{-1}.

3 COLLISIONAL DYNAMICS

For the various symmetries of ND_2H and ND_3[2] the calculations aim at providing rate coefficients up to $T = 50$ K and for rotational energy levels below ∼100 cm^{-1}. More precisely, in the case of ND_2H, we thus provide rate coefficients for the levels up to $J_\tau = 3_3$. For the para symmetry of ND_3, we consider the levels up to $J_K = 4_0$ and for the ortho symmetry, up to $J_K = 4_1$ (see Table 1).

[2] The ND_2H molecule is an asymmetric top which can be described by the quantum numbers J, K_a and K_c. In what follows, we use the pseudo-quantum number $\tau = K_a$–K_c and adopt the notation J_τ to describe the rotational structure. The ND_3 molecule is a symmetric top which is described by the J and K quantum numbers and we hence label the levels as J_K. For both molecules, the umbrella vibrational motion further splits every rotational level in two energy levels. We then introduce the ϵ quantum number in order to distinguish the levels in every doublet. With $\epsilon = \pm 1$, the ND_2H and ND_3 energy levels are then, respectively, labelled as $J_\tau^\pm$ and $J_K^\pm$ (see details in Appendix A).

Table 1. Theoretical energy levels of the three ND_3 symmetries, for the first 20 energy levels. For each symmetry, we give the quantum numbers J^{ϵ}_{K} and the energy in cm^{-1}.

o–ND_3		p–ND_3		m–ND_3	
1^-_1	8.27	0^+_0	0.05	0^+_0	0.00
1^+_1	8.32	1^+_0	10.29	1^+_0	10.34
2^+_2	22.78	2^+_0	30.91	2^+_0	30.86
2^-_2	22.83	3^+_3	43.55	3^-_3	43.55
2^+_1	28.84	3^-_3	43.60	3^+_3	43.60
2^-_1	28.89	3^+_0	61.71	3^+_0	61.76
3^-_2	53.64	4^-_3	84.69	4^+_3	84.69
3^+_2	53.69	4^+_3	84.74	4^-_3	84.74
3^-_1	59.69	4^+_0	102.90	4^+_0	102.85
3^+_1	59.74	5^+_3	136.12	5^-_3	136.12
4^+_4	70.56	5^-_3	136.17	5^+_3	136.17
4^-_4	70.61	6^-_6	143.34	6^+_6	143.34
4^+_2	94.78	6^+_6	143.39	6^-_6	143.39
4^-_2	94.83	5^+_0	154.28	5^+_0	154.33
4^+_1	100.84	6^-_3	197.83	6^+_3	197.83
4^-_1	100.89	6^+_3	197.88	6^-_3	197.88
5^-_5	103.83	7^+_6	215.34	7^-_6	215.34
5^+_5	103.88	7^-_6	215.39	7^+_6	215.39
5^-_4	121.99	6^+_0	216.04	6^+_0	215.99
5^+_4	122.04	7^+_3	269.83	7^-_3	269.83

Depending on the deuterated isotopologue, we either solved the collisional dynamics using the MOLSCAT[3] computer code or HIBRIDON[4] package which includes the treatment of both inversion motion and non-spherical linear collider. The former was used to treat the ND_2H–H_2 system, since we neglected the inversion motion for this particular isotopologue. The inversion motion splits every rotational level in two rotation–inversion energy levels, the splitting being of the order of $\sim$0.4 cm^{-1} for ND_2H. However, the two levels of every doublet are associated with different ND_2H nuclear–spin symmetries, either the ortho or para species, which are not connected through inelastic collisions. Hence, by neglecting the inversion motion we consider a system which is suitable to describe both the ortho and para species, if we omit the small error (0.4 cm^{-1}) made in the estimate of the energy of the rotation–inversion state. The methodology of the corresponding calculations is similar to the recent study of the NH_2D–H_2 collisional system (Daniel et al. 2014). In the case of ND_2H, we followed the description adopted in Wiesenfeld et al. (2011), which is based on the spectroscopic parameters given by Coudert, Valentin & Henry (1986) and Lucia & Helminger (1975). Hence, we described the energy levels adopting the rotational constants $A = 5.3412$, $B = 7.4447$ and $C = 3.7533$ cm^{-1} and the centrifugal terms $D_{JJ} = 3.346\,10^{-4}$, $D_{JK} = -4.931\,10^{-4}$ and $D_{KK} = 2.164\,10^{-4}$, these values being given in the II^r representation (W. Gordy 1984) suitable to MOLSCAT.

In the case of ND_3, two levels of a doublet can pertain to the same symmetry and thus can be connected through collisions. The MOLSCAT code could be used to treat such a problem, but only in the case of a spherical collider, like He or p–H_2 restricted to its fundamental rotational level $J_2 = 0$. Since our calculations aim at including the first excited state of p–H_2 (i.e. $J_2 = 2$), we used the HIBRIDON package which includes the possibility of treating the inversion motion in the case of a non-spherical collider. We checked the consistency of the results obtained with the two codes, for the collisions of o–ND_3 with H_2 ($J_2 = 0$) and we could verify that the cross-sections agree with an accuracy typically of the order of the per cent.

To define the ND_3 energy structure, we adopted the rotational constants $A = B = 5.142676$ and $C = 3.124616$ cm^{-1} and set the inversion splitting at a constant value of 0.05 cm^{-1}. The corresponding energy levels are given in Table 1. As can be seen in this table, the energy levels associated with the para and meta symmetries of ND_3 are mostly identical. The only differences between the two sets of energies are found for the $K = 0$ levels. This similarity entails that the cross-sections associated with the two symmetries will be roughly identical for a given $J^{\epsilon}_{K} \rightarrow J'^{\epsilon'}_{K'}$ transition. Indeed, the coupling terms that enter the dynamic equations are identical for the two symmetries and the only differences in the two sets of equations will thus come from the differences in the energy levels. These similarities are verified in our state-to-state cross-sections performed at a few energies. Cross-sections involving levels with both initial and final $K \neq 0$ differ at most by 1 per cent. For transitions that involve levels with $K = 0$, the differences may be higher but never exceed 5 per cent. Hence, we chose to perform calculations for only one symmetry, i.e. for p–ND_3. Full details on the spectroscopy of ND_3 are presented in Appendix A.

The accuracy of the cross-sections is assessed by a few test calculations where we checked the convergence against the step of integration used to propagate the wavefunctions, and the number of energy levels considered during the propagation. These parameters are summarized in Table 2 for ND_2H and Table 3 for ND_3. In the case of ND_3, the integration step is not reported since we used a single value of 0.1 a_0 at every energies. The parameters quoted in these tables ensure a convergence better than 5 per cent at all energies. In these tables, we also report the step between two consecutive energies. These values ensure a good characterization of the resonances, for the transitions between levels under consideration. For both ND_2H and ND_3, all the calculations were performed within the close–coupling formalism. Recently, Tkáč et al. (2015) reported quantum dynamical calculations for the ND_3–H_2 collisional system, with the aim of testing the PES against experimental

Table 2. Parameters that describe the MOLSCAT calculations performed for ND_2H–H_2, i.e. the step between the consecutive total energies used to characterize the cross-sections (second column), the STEPS parameter (third column) and the size of the rotational basis (fourth column).

Energy range (cm^{-1})	Step in energy (cm^{-1})	STEPS	JMAX
< 25	0.1	40	7
25–60	0.1	20	7
60–80	0.1	10	7
80–110	0.1	10	8
110–155	0.2	10	8
155–250	0.5	10	8
250–400	1	10	8

[3] J. M. Hutson and S. Green, MOLSCAT computer code, version 14 (1994), distributed by Collaborative Computational Project No. 6 of the Engineering and Physical Sciences Research Council (UK).

[4] HIBRIDON is a package of programs for the time-independent quantum treatment of inelastic collisions and photodissociation written by M. H. Alexander, D. E. Manolopoulos, H.-J. Werner, B. Follmeg, Q. Ma and P. J. Dagdigian, with contributions by P. F. Vohralik, D. Lemoine, G. Corey, R. Gordon, B. Johnson, T. Orlikowski, A. Berning, A. Degli-Esposti, C. Rist, B. Pouilly, G. van der Sanden, M. Yang, F. de Weerd, S. Gregurick, J. Klos and F. Lique. More information and/or a copy of the code can be obtained from the web site http://www2.chem.umd.edu/groups/alexander/hibridon/hib43.

Table 3. Parameters that describe the HIBRIDON calculations performed for the ortho and para symmetries of ND_3–H_2, i.e. the step between the consecutive total energies used to characterize the cross-sections (second column), and the size of the rotational basis given by the highest rotational quantum number (third column) and the cut in energy (fourth column).

Energy range (cm^{-1})	Step in energy (cm^{-1})	JMAX	E_{cut}
< 30	0.1	6	$+\infty$
25–65	0.1	7	$+\infty$
65–105	0.1	8	650
105–150	0.1	9	700
150–200	0.1	9	750
200–300	0.5	10	800
300–450	2.0	10	800

differential cross-sections. These comparisons were performed at total energies above 430 cm^{-1}. They assessed the convergence of their calculations with respect to the size of the rotational basis of the two rotators and, in particular, they found that omitting the $J_2 = 4$ energy level of p–H_2 can lead to misestimate the cross-sections by ∼25 per cent, for transitions associated with the $J_2 = 0 \rightarrow 0$ H_2 state-to-state transitions. Hence, we checked the accuracy of our calculations by testing the influence of the size of the H_2 rotational basis, at various total energies between 200 and 400 cm^{-1}. We find that below 400 cm^{-1}, the cross-sections were affected by less than 5 per cent due to the truncation of the p–H_2 rotational basis to $J_2 = 0, 2$. At 400 cm^{-1}, we indeed found that some transitions were more largely affected, with inaccuracies of up-to ∼35 per cent. However, less than 5 per cent of the total number of transitions are affected by errors greater than 5 per cent. Moreover, the corresponding cross-sections are the lowest in magnitude, i.e. lower than 0.001 $Å^2$, the highest cross-sections being of the order of 10 $Å^2$ at this total energy. Hence, given the low influence of the $J_2 = 4$ energy level of p–H_2 for the range of energy considered in this work, and since the inclusion of this level would considerably raise the calculation time, we chose to restrict the rotational levels of H_2 to $J_2 = 0, 2$.

4 RATE COEFFICIENTS

The de-excitation rate coefficients for the rotation–inversion transitions were calculated by averaging the above cross-sections with a Maxwell–Boltzmann distribution that describes the distribution of velocity of the molecules in the gas (see e.g. equation 5 in Wiesenfeld et al. 2011). The rate coefficients were thus obtained for temperatures in the range 5–50 K and for all transitions involving NHD_2 levels below 82 cm^{-1} (i.e. up to $J_\tau = 3_3$) and ND_3 levels below 103 cm^{-1} (i.e. up to $J_K = 4_0$ and 4_1 for the para and ortho species, respectively).

Since the hyperfine structure due to the nitrogen nuclei (^{14}N) is resolved observationally (see Section 6), rate coefficients for the hyperfine transitions are also required. The recoupling theory now routinely employed for linear species (see e.g. Daniel, Dubernet & Meuwly 2004; Daniel et al. 2005; Kalugina & Lique 2015) has not yet been extended to non-linear molecules for which only the statistical approximation is possible. In this approach, it is assumed that the hyperfine de-excitation rate coefficients are proportional to the degeneracy $(2F' + 1)$ of the final hyperfine level and completely independent of the initial hyperfine level. This corresponds to a statistical reorientation of the quantum number F after collision and it is also called the M_j randomizing limit or proportional approach. It has been shown to be inaccurate by large factors when predicting hyperfine individual rate coefficients (see e.g. Daniel et al. 2005; Faure & Lique 2012). On the other hand, when the opacity of the individual hyperfine lines is low (∼1), the hyperfine levels are populated according to their statistical weights and, in this regime, the statistical approximation is well adapted (Daniel et al. 2005; Faure & Lique 2012). As the hyperfine transitions of the deuterated isotopologues are usually optically thin, the statistical approximation should be accurate enough to model the spectra of NH_2D, NHD_2 and ND_3. Note that in radiative transfer models, the quasi-elastic J, $F \rightarrow J, F'$ rate coefficients are also needed. Unfortunately, these rate coefficients cannot be guessed from elastic rate coefficients, which are typically of the order of 10^{-9} cm^3 s^{-1}. Indeed, Faure & Lique (2012) showed that applying the proportional approach to elastic rate coefficients lead to overestimate the quasi-elastic rates by large factors, with respect to rate coefficients calculated with a recoupling method. Hence, in the radiative transfer calculations described in Section 6, we applied the proportional approach to a canonical rate of 10^{-10} cm^3 s^{-1} in order to obtain an estimate of the quasi-elastic rate coefficients.

The whole set of hyperfine rate coefficients will be available through the LAMDA (Schöier et al. 2005) and BASECOL (Dubernet et al. 2013) data bases.

5 DISCUSSION

To date, two sets of rate coefficients were computed for ND_2H. The first set considered He as a collider (Machin & Roueff 2007), while the second set was calculated for p–H_2 using a $J_2 = 0$ basis set (Wiesenfeld et al. 2011). Quite often, the collisions with He are used to emulate the rate coefficients with p–H_2. However, as for other molecular systems, the comparison between these two sets showed that the differences can be quite large, the rates with p–$H_2(J_2 = 0)$ being higher by a factor 3–30 depending on the transition.

In order to perform some comparison with these previous works, we considered the ND_2H–H_2 rate coefficients determined by Wiesenfeld et al. (2011), where data were computed for the nine first rotational energy levels and for temperatures in the range 5–35 K. These calculations only differ from the current ones in two points. First, in Wiesenfeld et al. (2011), the cross-sections were computed in part with the coupled–states approximation. In the current study, all the calculations were performed within the close–coupling formalism. Secondly, the present H_2 rotational basis includes the $J_2 = 2$ level, while it was reduced to $J_2 = 0$ in Wiesenfeld et al. (2011). As already commented in Daniel et al. (2014), increasing the H_2 basis can have a non-negligible effect on the estimate of the magnitude of the rate coefficients. In the case of NH_2D, it was found that using a $J_2 = 0$ basis rather than a $J_2 = 0, 2$ basis can lead to underestimating by a factor ∼3 the cross-sections of highest magnitude (see fig. 2 in Daniel et al. 2014). Moreover, in that study, it was already mentioned that the rates given by Wiesenfeld et al. (2011) should be accurate to within a factor ∼3. Such a factor was guessed from a few preliminary calculations and considering the behaviour of a reduced set of cross-sections (see fig. 9 in Daniel et al. 2014). With the current data, the comparison can be extended and done on more quantitative grounds. In Fig. 1, we show the ratio between the two sets of rate coefficients as a function of the magnitude of the rate coefficients. From this figure, it can be seen that the largest differences are found for the rates of highest magnitude. This is similar to what was already observed in the NH_2D–H_2 collisional system. Additionally, the alteration of the rates of highest magnitude is at most of a factor ∼2.5, which is of the same order of magnitude as for the NH_2D–H_2 collisional system.

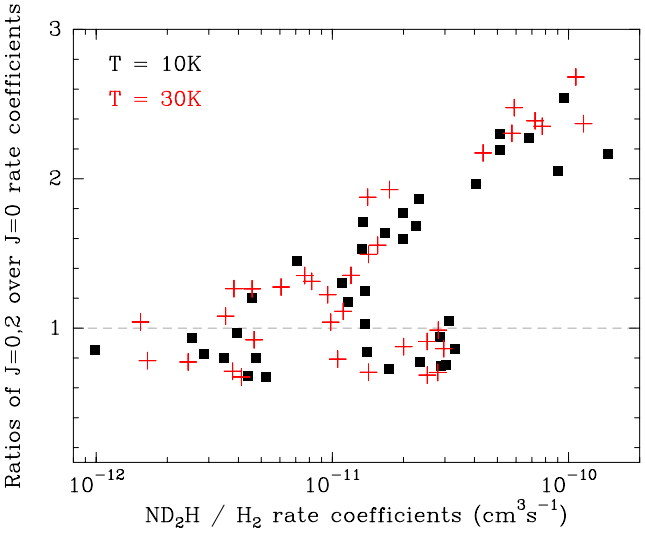

Figure 1. Ratio between the ND_2H/H_2 rate coefficients calculated in this work with a $J = 0,2$ basis for H_2, with those of Wiesenfeld et al. (2011) that were obtained with a $J = 0$ basis. The comparison considers the levels up-to $J_\tau = 2_2$ and is performed at $T = 10$ K (black points) and $T = 30$ K (red crosses).

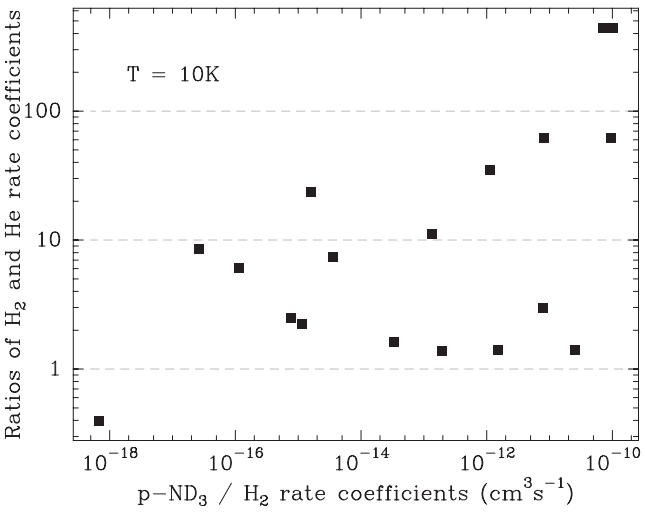

Figure 2. Ratio of the H_2 over He rate coefficients of p–ND_3. The comparison considers the levels up-to $J^\epsilon_K = 4^-_3$ and is performed at $T = 10$ K.

The calculation of ND_3–He rate coefficients was a goal of the PhD thesis of L. Machin (Machin 2006, these unpublished rate coefficients are given in table 5.3 of the thesis manuscript)[5]. As already evidenced for the NH_2D and NHD_2 isotopologues, the differences between the He and H_2 rate coefficients are large (see fig. 8 in Daniel et al. 2014). In Fig. 2, we plot the ratio of the H_2 and He rate coefficients, at a temperature $T = 10$ K and for the levels up to $J^\epsilon_k = 4^-_3$. As for NH_2D and NHD_2, the ratios are in the range 1–100 and the largest differences are obtained for the highest rate coefficients. Interestingly, the calculations of Machin with He were performed for both the para and meta symmetries (however, the meta symmetry was misleadingly referenced as ortho in that work). Machin could thus check that the rate coefficients for the para and meta species agree with a good accuracy, as expected. In fact, he found that at temperatures higher than 50 K, the agreement is better than a few per cent. The comparison at $T = 10$ K shows larger differences, but most of the rate coefficients agree to within 20 per cent (in table 5.3 of the manuscript, the $1^+_0 \rightarrow 3^-_3$ transition is the only transition that shows a higher ratio, i.e. ∼2). These differences in the para and meta rate coefficients were attributed to differences in the resonance structure. In Section 3, we mentioned that we performed some test calculations at some specific energies and we could verify that at these energies, the meta and para cross-sections agree within a few per cent. However, as in the case of the collisions with He, we cannot discard that the resonance structure for the two symmetries could induce larger differences, but not above ∼20 per cent, which is the typical accuracy of the present rate coefficients.

[5] https://tel.archives-ouvertes.fr/tel-00128133

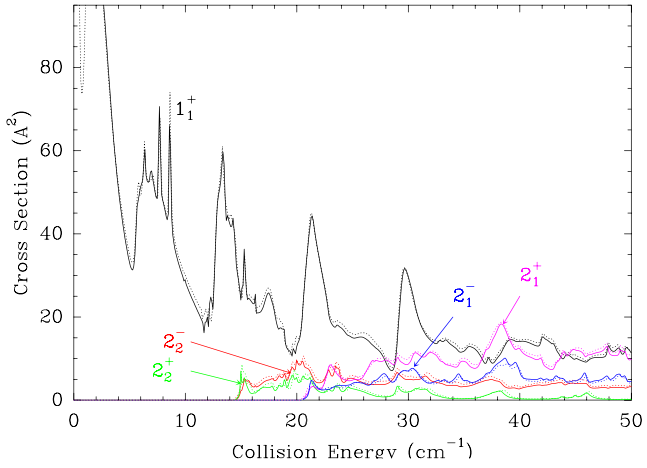

Figure 3. Cross sections for o–ND3 that originate from the 1^-_1 level. This figure can directly be compared to fig. 13 of Ma et al. (2015) and the cross-sections obtained in the latter study are reported as dotted lines.

Recently, Ma et al. (2015) reported dynamical calculations for the ND_3–H_2 system that were performed on the same PES as the current calculations. These two sets of calculations were performed independently and with a different focus. While in the current case, we are interested in providing collisional rate coefficients, Ma et al. (2015) put emphasis on the description of the resonance features in order to probe the possibility of characterizing these resonances in future experiments. Since the energy, strength and shape of the resonances depend strongly on the accuracy of the PES, this would provide a test of the accuracy of the PES of Maret et al. (2009) and hence, would give an estimate of the accuracy we could expect for the rate coefficients. In Fig. 3, we give the cross-sections of o–ND_3 that originate from the 1^-_1 level. This figure is similar to fig. 13 of Ma et al. (2015) and in the current figure, the cross-sections obtained by Ma et al. (2015) are reported as dotted lines. The overall agreement between the two sets of calculations is very good, even if there remains some small differences in the description of the resonances. These differences do not exceed a few per cent and presumably originate from the respective accuracy of the two collision dynamics calculations.

6 ASTROPHYSICAL MODELLING

The rate coefficients described in the previous sections are a key ingredient for astrophysical models interpreting the deuterated ammonia inversion/rotational lines observed from far-infrared to centimetre wavelengths. Such observations of the NH_2D, ND_2H and ND_3 isotopologues were reported and analysed by Tiné et al. (2000),

Roueff et al. (2000), Saito et al. (2000), Lis et al. (2002b), van der Tak et al. (2002), Roueff et al. (2005), Lis et al. (2006) and Gerin et al. (2006), but the lack of rate coefficients hampered the analysis, which thus relied on simplifying assumptions. In some cases, the recourse to such simplification leads to discrepancies, as outlined by Lis et al. (2006). Indeed, it was then shown that an local thermodynamic equilibrium (LTE) analysis applied to two rotational lines of o–ND_2H, at 336 and 389 GHz, gives inconsistent column density estimates. In the case of the observations towards the pre-stellar cores 16293E or B1b, it was found that the two estimates disagree by factors of ∼3 and 6, respectively.

In what follows, we reconsider the observations available towards B1b and 16293E, in light of the newly calculated ND_2H and ND_3 rate coefficients presented here, as well as the NH_2D/H_2 rate coefficients described in Daniel et al. (2014). The molecular excitation and radiative transfer is solved with the 1DART code described in Daniel & Cernicharo (2008). As in Daniel et al. (2013), we report column densities, which are calculated by counting the number of molecules across the diameter of the spheres that describe the sources. These column densities are not tied to any particular molecular transition and hence or not averaged over a particular telescope beam size. Such beam averaged column densities are often introduced when estimating molecular column densities and in what follows, we will sometimes introduce it for the sake of comparison with previous results.

6.1 Barnard 1b

B1b, located at 235 pc in the Perseus molecular cloud, is a region of active low-mass star formation. The region around B1b has been the subject of many observational studies (see references in Daniel et al. 2013) and consists of two objects, B1b–N and B1b–S (Hirano et al. 1999), whose evolutionary states are still under debate. Currently, B1b–N is thought to be in the first hydrostatic core stage while B1b–S seems to be a slightly more evolved object (Hirano & Liu 2014; Gerin et al. 2015).

6.1.1 NH_2D

The physical structure adopted for this source (i.e. dust and gas temperatures, H_2 density) is taken from Daniel et al. (2013), where it was inferred from the analysis of 850 μm and 1.3 mm continuum observations. In the latter study, the map of the o–NH_2D $1_{1,1}$–$1_{0,1}$ emission was already analysed by solving the molecular excitation. However, the rate coefficients for the NH_2D–H_2 system were not available at that time and the analysis thus relied on the NH_2D–He rate coefficients (Machin 2006), that were subsequently scaled. We refer the reader to the discussion in Daniel et al. (2013) for the details that concern the scaling of the rates. More recently, Daniel et al. (2014) reported rate coefficients for the NH_2D–H_2 system. Using these new rate coefficients with the o–NH_2D abundance profile given in Daniel et al. (2013), we find that it leads to overestimate the line intensity by a factor ∼2. This illustrates the inaccuracy introduced by the scaling of the rate coefficients. We thus re-analyse the o–NH_2D and o–$^{15}NH_2D$ data available towards B1b with the same methodology as in Daniel et al. (2013). In particular, we note that the B1b is a complex region, with two cores separated by ∼20 arcsec, which have V_{LSR} that differ by ∼1 km s^{-1}. Hence, to model the spectra, we follow the methodology described in Daniel et al. (2013): we use a 1D spherical model, adopt a V_{LSR} ∼ 6.7 km s^{-1} and constrain the models by fitting the blue part of the spectra. The estimate of the NH_2D abundance profile across the core is constrained thanks to the o–NH_2D $1_{1,1}$–$1_{0,1}$ emission map and the comparison between the model and observations is given in Fig. 4. The corresponding o–NH_2D abundance profile is reported in red in Fig. 5. The confidence zone, as defined in Daniel et al. (2013), is indicated as grey area. In this figure, the abundance profile derived by Daniel et al. (2013) is shown in blue. Finally, the o–$^{15}NH_2D$ data observed towards the central position was also re-analysed. The comparison of the models and observations for the two isotopologues at this position are given in Fig. 6.

The previous estimate for the o–NH_2D column density made by Daniel et al. (2013) was $\log(N) = 14.73^{+0.12}_{-0.08}$. With the new rate coefficients, this value is revised to $\log(N) = 14.76^{+0.10}_{-0.14}$. For o–$^{15}NH_2D$, the column density was previously estimated to $\log(N) = 12.37^{+0.33}_{-0.11}$ while the current estimate is $12.31^{+0.20}_{-0.16}$. The corresponding isotopologue column density ratio, previously estimated to 230^{+105}_{-55} is now 280^{+120}_{-100}.

In the case of the p–NH_2D spin isomer, the abundance was constrained using a mini-map of the $1_{1,1}$–$1_{0,1}$ line at 110 GHz, observed at the IRAM 30 m telescope, and the $1_{1,0}$–$0_{0,0}$ line at 494 GHz, observed with Herschel. These latter data were obtained using the HIFI instrument (de Graauw et al. 2010) on Herschel (Pilbratt et al. 2010), in the context of the open time program OT2_dlis_3 (Herschel observation ID 1342248917). The data were taken in the frequency-switching mode, were processed using the standard HIFI data reduction pipeline and the resulting spectra were subsequently reduced using the GILDAS CLASS software package. The FWHM HIFI beam size is ∼44 arcsec at 492 GHz and the main beam efficiency is 62 per cent.[6]

By using an overall scaling of the o–NH_2D abundance profile, we managed to obtain a reasonable fit of the p–NH_2D observations, although the line shape of the $1_{1,0}$–$0_{0,0}$ transition is not correctly reproduced. Indeed, the best-fitting model predicts self-absorption features which are not observed (see right-hand panel in Fig. 6). Some alternative models were tried in order to improve the fit, but we could not find a model that would considerably improve the comparison with the observations. We thus kept the simplest model, i.e. the model where the p–NH_2D abundance is scaled from the o–NH_2D abundance profile. The OPR derived from the modelling is $4.8^{+3.2}_{-2.0}$. This ratio is higher than the ratio predicted through statistical considerations, i.e. 3, but, compatible given the large error bars. Additionally, we note that examining the possible scenarios relative to the NH_2D formation, a ratio of 3 would be expected in the case of formation on grains (with $T_g \geq 10$ K) while a ratio <3 is expected if the formation occurs in the gas phase (Sipilä et al. 2015). Note, however, that it was shown by Persson et al. (2015) that, in the case of NH_2, the interconversion between ortho and para states due to reactive collisions with H atoms is an efficient process that may substantially alter the NH_2 OPR. Such process is, however, generally not included in the gas-phase formation models due to the lack of either theoretical or experimental value for the reactive rate coefficients. Finally, to date, OPR higher than 3 are not expected for NH_2D. Although Shah & Wootten (2001) reported similar values, we believe that the accuracy of the analysis is influenced by the high opacity of the line, which introduces uncertainties in the estimate of the abundance profile. This is illustrated by the models shown in Fig. 7. In this figure, we show a model for the 110 GHz line where the p–NH_2D abundance profile is set identical

[6] http://herschel.esac.esa.int/twiki/pub/Public/HifiCalibrationWeb/HifiBeamReleaseNote_Sep2014.pdf

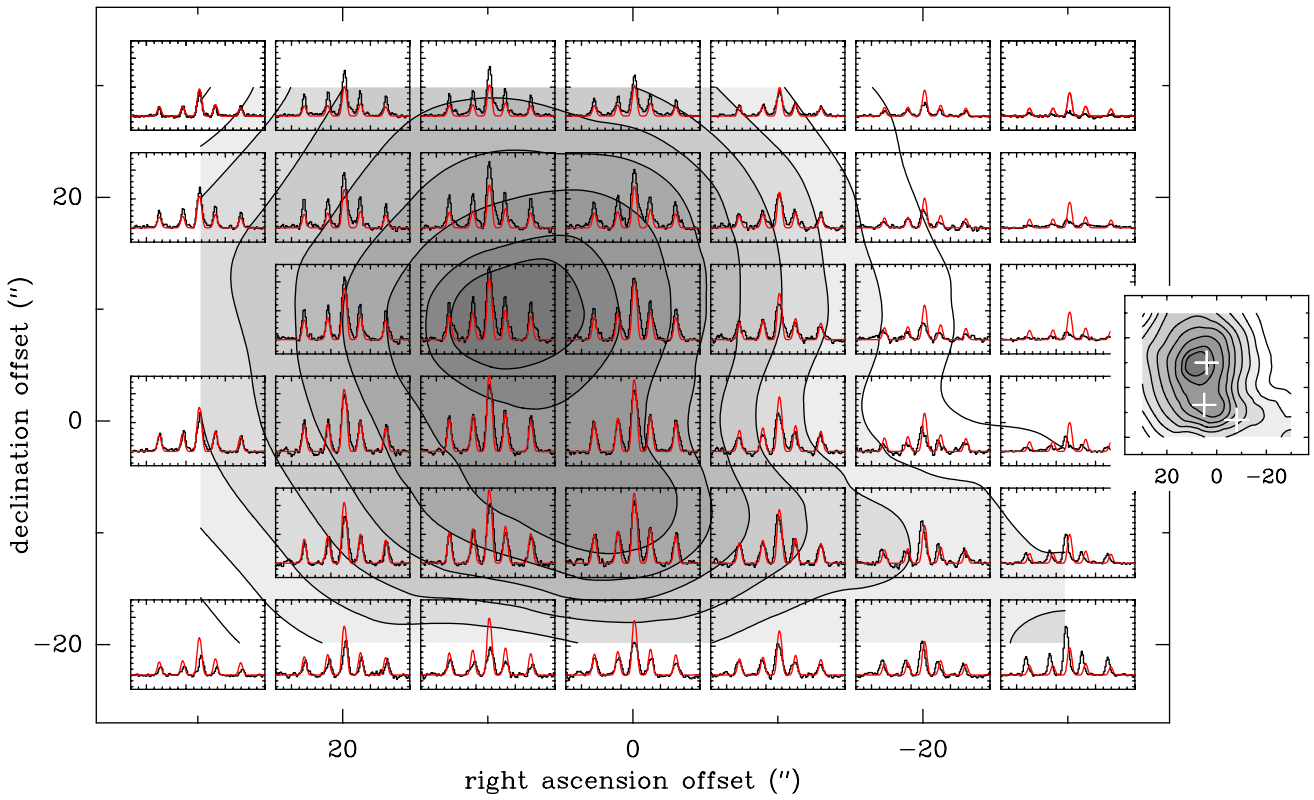

Figure 4. [The labels of the axis were modified] Comparison between model (red curves) and observations (histograms) for the o–NH_2D $1_{1,1}$–$1_{0,1}$ line towards B1b.The inset map on the right shows the isocontours with the same scale for the right ascension and declination. The white crosses indicate the position of the B1-bN and B1-bS sources identified by Hirano et al. (1999), as well as the *Spitzer* source reported by Jörgensen et al. (2006).

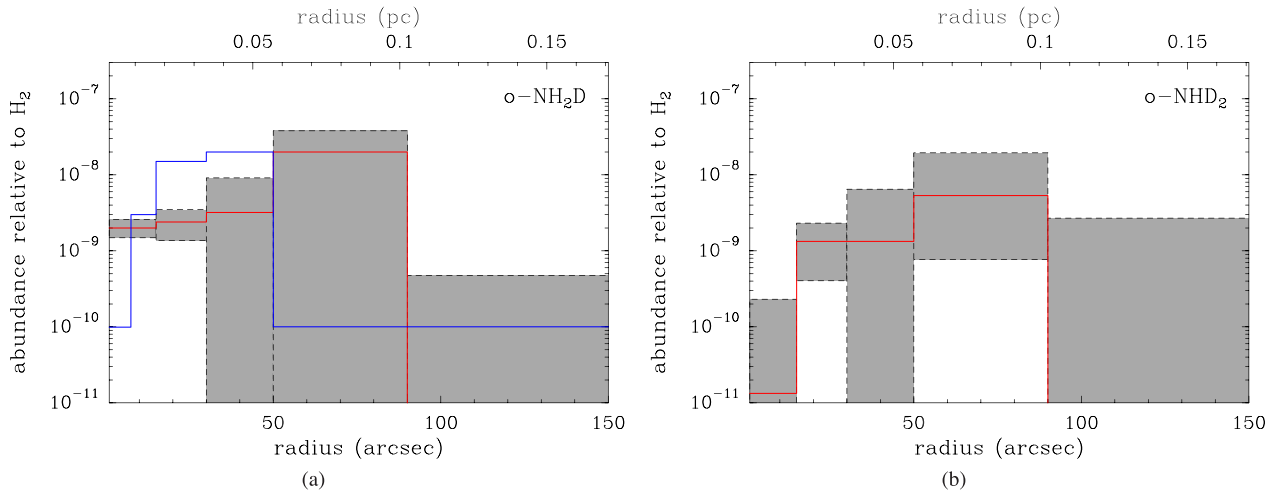

Figure 5. (a) Abundance profile of o–NH_2D (red curve) as a function of radius in the pre-stellar core B1b. The grey areas show the confidence zone for the abundance at every radius. The abundance profile derived by Daniel et al. (2013) is indicated as a blue curve. (b) Abundance profile of o–NHD_2 (red curve) as a function of radius.

to the o–NH_2D profile (blue curve). The corresponding intensities are compared to the model adopted for B1b (red dashed curve). The fact that the intensity does not scale linearly with the column density is emphasized through the comparison with the model where the intensities are scaled according to the OPR (red curve). In particular, it can be seen that the hyperfine satellites are in a regime of opacity where they still scale proportionally to the column density. The central component is however opaque and the two models differ by a factor ∼2. From this comparison, it can be inferred that if we consider the ratio of integrated intensities of the 86 and 110 GHz lines, this ratio will only give a lower limit to the OPR. For the (0 arcsec,0 arcsec) position, this ratio is ∼2.9. Finally, if we only consider the most optically thin hyperfine satellites, their integrated intensity ratio should be closer to the actual OPR. Considering these components, we obtain an integrated intensity ratio 3.5 ± 0.2. To conclude, the various ways of deriving the OPR of NH_2D rule out a ratio lower than 3 and therefore favour the grain surface formation processes.

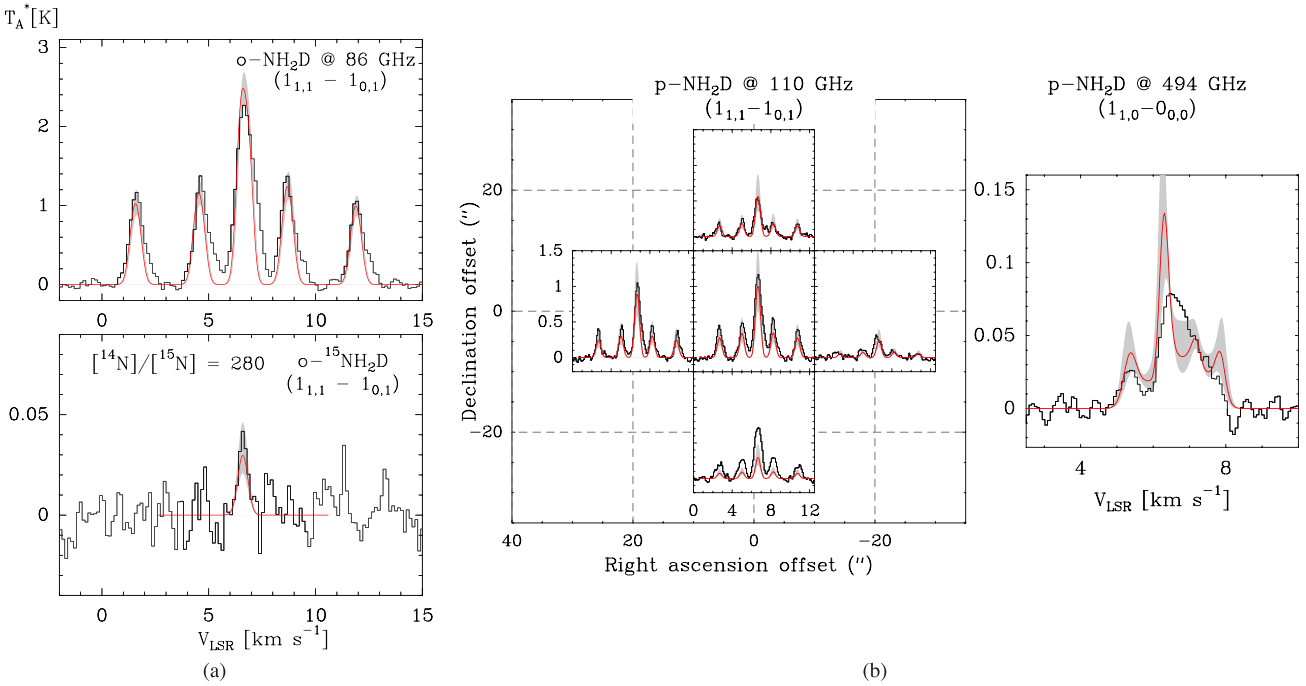

Figure 6. [The labels of the axis of the mini-map were modified] Comparison between model (red curves) and observations (histograms), in the T_A^* scale, for the NH_2D lines observed towards B1b: (a) o–NH_2D and o–$^{15}NH_2D$ $1_{1,1}$–$1_{0,1}$ lines (b) mini-map of the p–NH_2D $1_{1,1}$–$1_{0,1}$ line (left-hand panel) and single point observation of the $1_{1,0}$–$0_{0,0}$ line (right-hand panel)

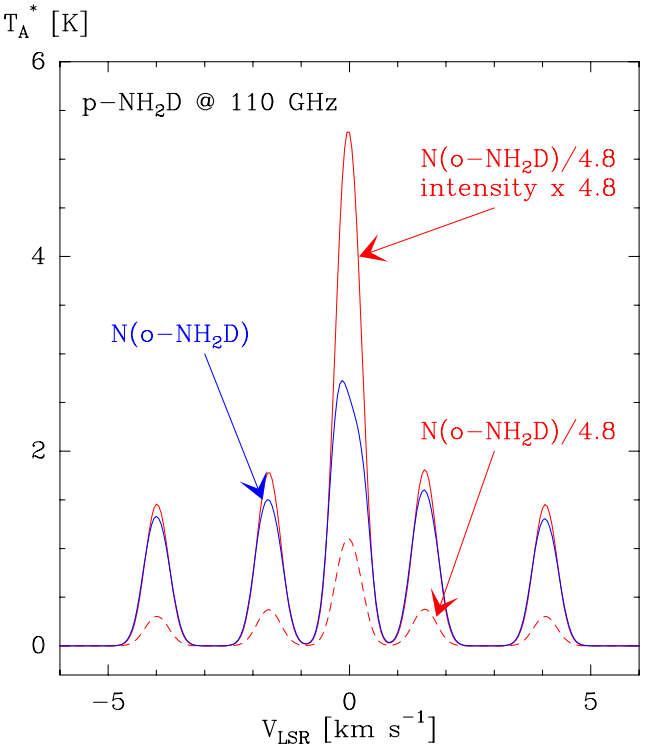

Figure 7. Models for the p–NH_2D 110 GHz transition. The blue curve gives the intensity we would obtain with a p–NH_2D abundance profile identical to that of o–NH_2D. The red dashed curve corresponds to the model adopted to reproduce the p–NH_2D 110 and 494 GHz lines, with an OPR of 4.8. The red curve corresponds to the same model with the intensity multiplied by a factor 4.8.

Considering these various estimates and since, to date, the highest value expected for the OPR of NH_2D is 3, we use this latter value, in what follows, to derive the NH_2D total column density. The total NH_2D column densities is thus $\log(N) = 14.88^{+0.10}_{-0.14}$.

6.1.2 NHD_2

Using the same methodology as for NH_2D, we re-analysed the o–NHD_2 (single position) observations published in Lis et al. (2006). The spectroscopy of o–NHD_2 was obtained from the *splatalogue* data base where the hyperfine structure spectroscopy corresponds to the data published in Coudert & Roueff (2006, 2009). As a first guess, we used the NH_2D abundance profile discussed in the previous section, and tried to scale it by a constant value in order to reproduce the two observed lines at 336 and 389 GHz. By doing so, we could not find a reasonable model. Indeed, a model that fits the 336 GHz line could be obtained by scaling down the o–NH_2D abundance by a factor 4.5. However, this would lead to a model where the integrated area of the 389 GHz line would be overestimated by a factor ∼3. As stated by Lis et al. (2006), the 389 GHz line has a higher critical density than the 336 GHz line. Hence, in order to simultaneously fit the two o–NHD_2 lines, the NH_2D abundance profile has to be modified with a global shift of the abundance towards lower densities, i.e. larger radii. Such a model corresponds to the abundance profile given in Fig. 5 (right-hand panel) and the corresponding fit of the observations is shown in Fig. 8. As an alternative to this modification, we checked other possibilities that would enable to define NH_2D and NHD_2 abundance profiles that would only differ by a scaling factor. We found that assuming a constant gas temperature around 10 K would allow such a solution. However, given the constraints obtained on the dust temperature across the B1b region (see Daniel et al. 2013) and given the high densities in the innermost part of the core, this solution was discarded.

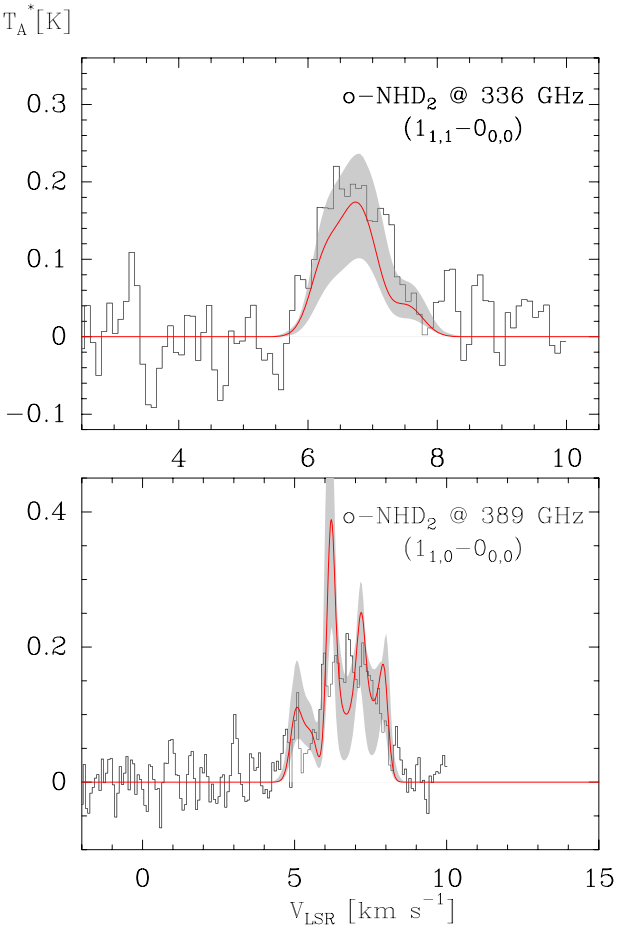

Figure 8. Comparison between model (red curves) and observations (histograms) for the o–NHD_2 lines at 336 and 389 GHz observed towards B1b.

The NHD_2 observations in B1b were already discussed in Lis et al. (2006). As mentioned earlier, in the latter study, the column density estimated separately from the 336 or 389 GHz lines, using an LTE approximation, were found to disagree by a significant factor. Indeed, these beam averaged column densities were, respectively, found to be 1.6×10^{14} and 2.9×10^{13} cm^{-2}, i.e.log(N) = 14.20 and 13.46. Here, the o–NHD_2 column density is estimated to log(N) = $13.90^{+0.38}_{-0.26}$. Finally, a previous analysis by Lis et al. (2006) have shown that in B1b, the OPR is consistent with the ratio of the nuclear–spin statistical weights, i.e. 2:1, within error bars. With such a ratio, the total NHD_2 column densities is thus log(N) = $14.08^{+0.38}_{-0.26}$.

6.1.3 ND_3

To model the ND_3 transition (see Fig. 9), we scaled the o–NH_2D abundance profile by an overall factor. In fact, the exact shape of the abundance profile is not constrained since the observed line is optically thin and because observations are available only towards a single position. As a consequence, alternate abundance profiles would provide similarly good fits to the observations. Hence, the only parameter which is well constrained by the model is the column density. The m–ND_3 column density is estimated to log(N) = $12.71^{+0.17}_{-0.20}$. In a previous study, Lis et al. (2002b) reported a ND_3 column density of $2 \pm 0.9 \times 10^{12}$ cm^{-2}, i.e. log(N) = $12.30^{+0.16}_{-0.16}$. This value corresponds to the total ND_3 column density, i.e. which consider all the spin isomers, and is averaged over the beam size. With the current model, the column density averaged over a beam of 25 arcsec lead to a column density for m–ND_3 of 2.7×10^{12} cm^{-2}. Assuming, that the ortho, meta and para spin isomers are populated according to their spin statistical weights, i.e. 16:10:1, we obtain a total column density of 7.3×10^{12} cm^{-2} which is a factor ∼3.5 higher than the estimate of Lis et al. (2002b). Note however that in Lis et al. (2002b), the column density estimate assumes that the various spin isomers are thermalized at the gas temperature. At 5 and 10 K, this implies that ∼60 and 45 per cent of the molecules are, respectively, in the meta modification. In the current estimate, we assume that the proportion of molecules in the meta modification is independent of the temperature and is set at 37 per cent. Hence, a factor ∼1.5 in the two estimates comes from the hypothesis, respectively, made on the partition functions.

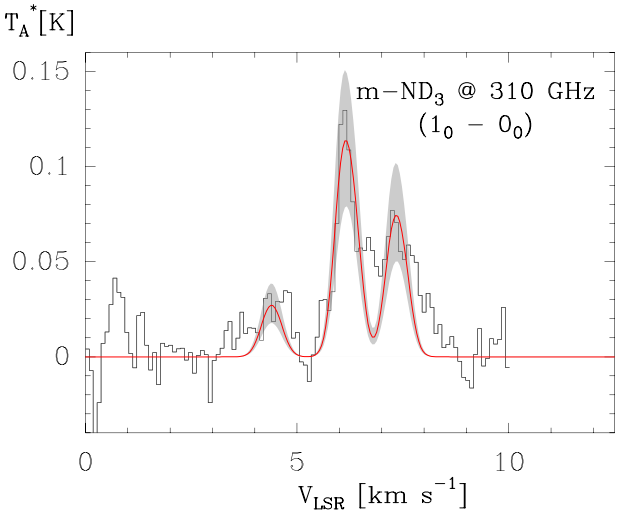

Figure 9. Comparison between model (red curves) and observations (histograms) for the m–ND_3 line at 309.9 GHz observed towards B1b.

Finally, assuming that the ortho, para and meta ND_3 states are populated according to the ratios 16:1:10, we derive log(N) = $13.14^{+0.17}_{-0.20}$.

6.1.4 Discussion

Deviations of the OPR from the statistical weights ratio are expected if the molecules form in the gas-phase owing to nuclear–spin selection rules. Nuclear–spin effects in the gas-phase have, however, a complex dependence on density, temperature and time (Faure et al. 2013; Rist et al. 2013; Sipilä et al. 2015). Here, we have thus assumed that the various nuclear–spin species of all four ammonia isotopologues are populated according to their spin statistical weights, in order to translate the observed column densities to total column densities. In the case of the main isotopologue of ammonia, the p–NH_3 column density was estimated to be log(N) = $14.74^{+0.25}_{-0.13}$ (Daniel et al. 2013), which translates to a total column density of log(N) = $15.04^{+0.25}_{-0.13}$ assuming a statistical OPR of 1:1.

The fractionation ratios derived from the current analysis are reported in the first entry of Table 4. Note that with respect to the previous estimate reported by Roueff et al. (2005) and displayed in this table, the current analysis leads to larger ratio, the updated values being higher by factors in the range 1–10. We thus obtain for Barnard 1b NH_2D/NH_3 ∼0.69, NHD_2/NH_2D∼0.16 and ND_3/NHD_2 ∼0.11. These ratios provide very useful constraints for

Table 4. Ratio of column density of the various isotopologues of NH_3, obtained for the B1b and 16293E molecular clouds. The column heading New refers to the current results while the column heading Old corresponds to the values reported by Roueff et al. (2005).

	$[NH_2D]/[NH_3]$		$[ND_2H]/[NH_2D]$		$[ND_3]/[NHD_2]$		$[ND_3]/[NH_3]$	
	Old	New	Old	New	Old	New	Old	New
B1b	0.23 ± 0.05	$0.69^{+0.24}_{-0.19}$	0.15 ± 0.03	$0.16^{+0.22}_{-0.03}$	0.033 ± 0.01	$0.11^{+0.09}_{-0.04}$	$1.1 \pm 0.5 \times 10^{-3}$	$1.3 \pm 0.6 \times 10^{-2}$
16293E	0.19 ± 0.05	–	0.22 ± 0.05	$0.21^{+0.08}_{-0.06}$	0.024 ± 0.01	$0.05^{+0.02}_{-0.01}$	$1.0 \pm 0.5 \times 10^{-3}$	–

astrochemical models and they should help, in particular, to disentangle between a gas-phase and a grain surface formation of the ammonia isotopologues. The gas-phase model of Roueff, Loison & Hickson (2015) was shown to reproduce the observed column density ratios of all four ammonia isotopologues in B1b and 16293E within a factor of 3. The updated observed value for NH_2D/NH_3 would be however underpredicted by a factor of ∼5. On the other hand, it is interesting to note that a purely statistical model[7] of grain surface formation (i.e. through statistical hydrogenation/deuteration of solid atomic nitrogen) reproduces the observed ratios within the error bars, provided that the accreting atomic D/H ratio is ∼0.2. Such a high value for the D/H ratio is actually predicted in regions with high density and heavy depletion, such as pre-stellar cores (Roberts, Herbst & Millar 2003). Clearly, more observations of the four ammonia isotopologues, in several other sources, as well as other related species such as ND and NHD, are necessary to make progress.

6.2 16293E

The IRAS 16293E source is a pre-stellar core located close to the IRAS 16293-2422 protostar. Hence, its physical and chemical properties are influenced by this source, mainly because of the interaction with the outflows that emanate from it (Castets et al. 2001; Lis et al. 2002a).

To model the emission of the ammonia isotopologues observed towards the 16293E core, we adopt the source structure described in Bacmann et al. (2015). Based on ground-based and space-based observations of the dust continuum emission at various wavelengths, the centre of the density profile is assumed to be at the position $\alpha_{2000} = 16^h32^m28^s.8$, $\delta_{2000} = -24°29'04''.0$ (Bacmann et al. 2015). The reference position of the observations is $\alpha_{2000} = 16^h32^m29^s.47$, $\delta_{2000} = -24°28'52''.6$ (Roueff et al. 2005; Lis et al. 2006).

In order to constrain the behaviour of the abundance, we start by considering the o–NHD_2 isotopologue, for which we have maps of the 336 GHz line emission obtained with APEX (Gerin et al. 2006), as well as CSO observations of the 336 and 389 GHz lines obtained close to the dust emission peak (Lis et al. 2006). As for the B1b modelling, it is confirmed that these two lines are good probes of the radial variations of the abundance profile, because of their respective critical densities and because of the difference of opacity of the lines.

6.2.1 NHD_2

The comparison between the model and observations for the 336 and 389 GHz lines is given in Fig. 10. The map of the 336 GHz line obtained with APEX is reported in Fig. 11. The abundance profile, which corresponds to these models, is given in Fig. 12.

[7] A purely statistical approach predicts the following ratios: $NH_2D/NH_3 = 3\times D/H$; $NHD_2/NH_2D = D/H$; $ND_3/NHD_2 = \frac{1}{3} \times D/H$.

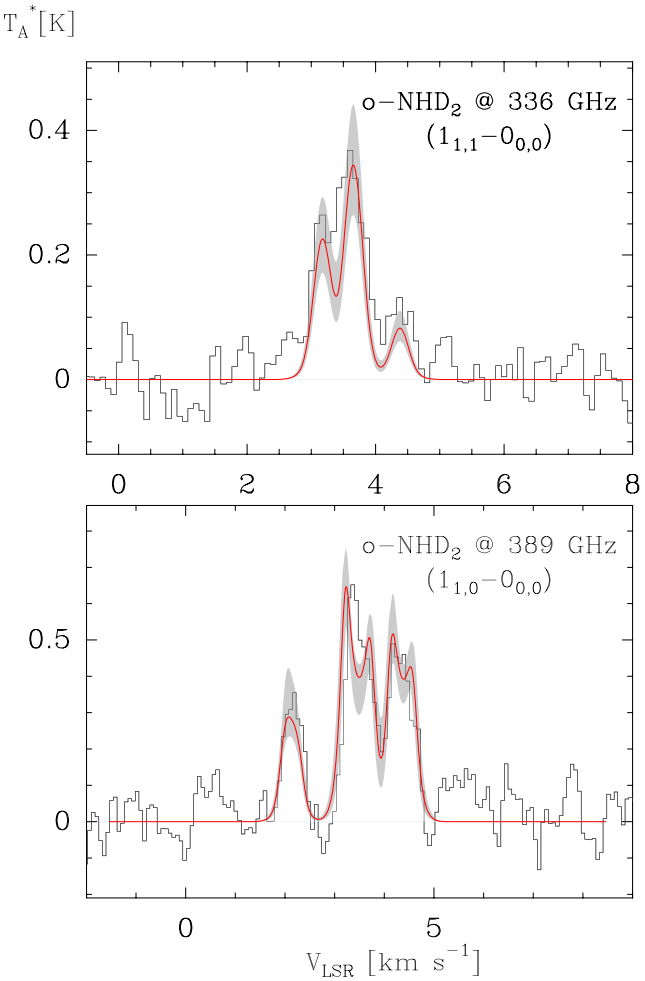

Figure 10. Comparison between model (red curves) and observations (histograms) for the o–NHD_2 line at 336 and 389 GHz observed with the CSO towards 16293E. The position observed is at an offset of (−10 arcsec,−10 arcsec) with respect to the reference position $\alpha_{2000} = 16^h32^m29^s.47$, $\delta_{2000} = -24°28'52''.6$.

As outlined in Gerin et al. (2006), the o–NHD_2 and the dust emission peak are offset by ∼10 arcsec. With the current spherical model, such an asymmetry cannot be taken into account and the model shown in Fig. 11 thus only reproduces qualitatively the overall behaviour of the o–NHD_2 emission. Finally, assuming an OPR of 2:1, i.e. given by the nuclear–spin statistical weights, we obtain a good fit to the APEX p–NHD_2 map. The comparison between model and observations is reported in Fig. 13. The OPR is similar to the one obtained by Gerin et al. (2006) where the abundance ratio was derived from the line intensity ratio, which is accurate in the case of optically thin lines.

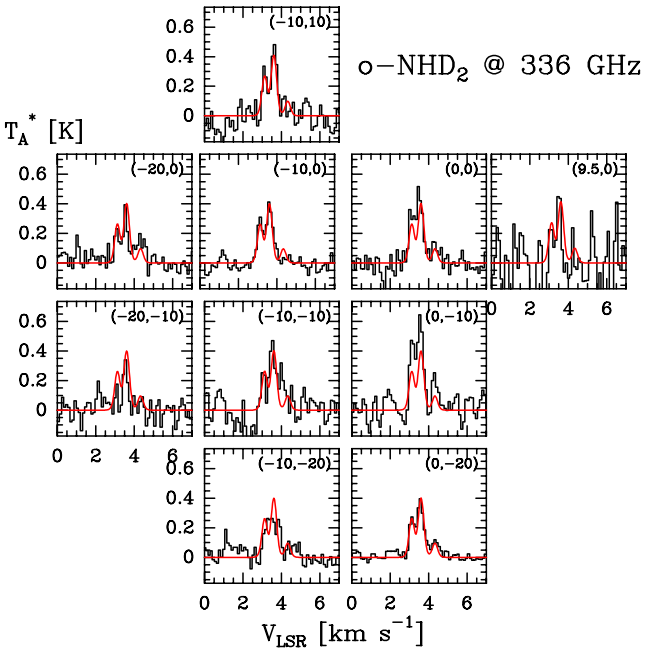

Figure 11. Comparison between model (red curves) and observations (histograms) for the o–NHD_2 line at 336 GHz observed with APEX towards 16293E. In each panel, the offset is indicated according to the reference position $\alpha_{2000} = 16^h32^m29\overset{s}{.}47$, $\delta_{2000} = -24°28'52\overset{''}{.}6$.

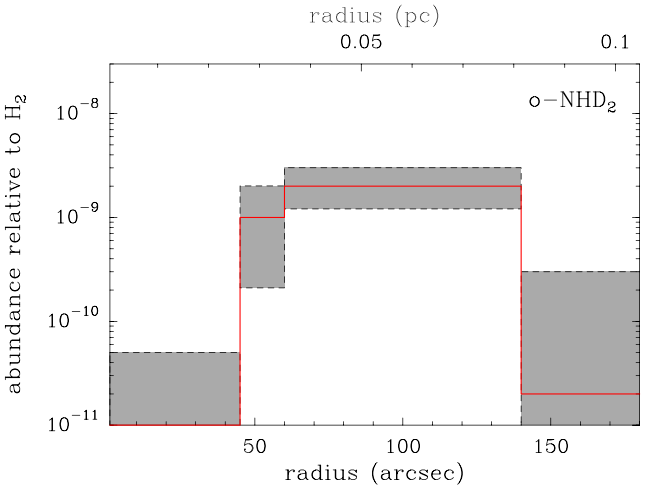

Figure 12. Abundance profile of o–NHD_2 (red curve) as a function of radius in the pre-stellar core 16293E. The grey areas show the confidence zone for the abundance at every radius.

The o–NHD_2 column density is $\log(N) = 13.82^{+0.14}_{-0.15}$ and with a 2:1 ratio between the ortho and para species, this gives a total column density of $\log(N) = 13.99^{+0.14}_{-0.15}$.

6.2.2 NH_2D

The o–NH_2D ($1_{1,1}$–$1_{0,1}$) line was observed at the single position $\alpha_{2000} = 16^h32^m29\overset{s}{.}47$, $\delta_{2000} = -24°28'52\overset{''}{.}6$, which is offset by ∼15 arcsec from the centre of our model. This o–NH_2D observation can be satisfactorily reproduced by applying an overall scaling factor to the o–NHD_2 abundance profile discussed in the previous section. The comparison between the model and observations is shown in Fig. 14.

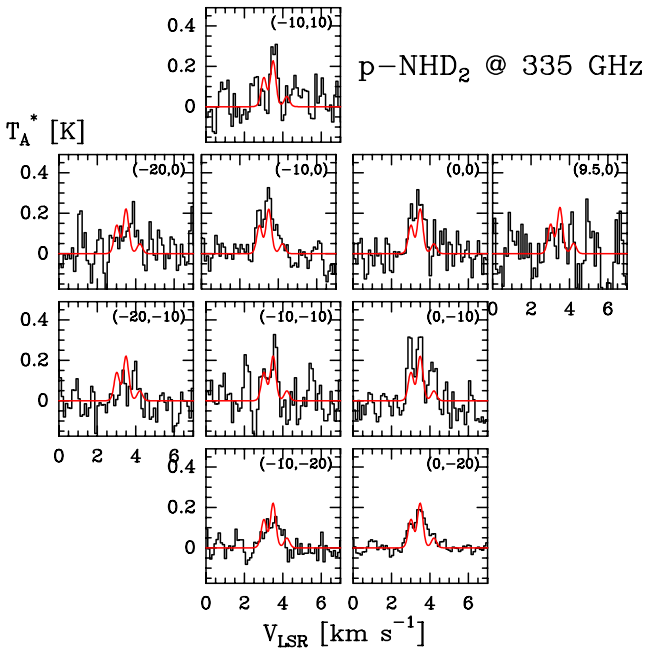

Figure 13. Comparison between model (red curves) and observations (histograms) for the p–NHD_2 line at 335 GHz observed with APEX towards 16293E. In each panel, the offset is indicated according to the reference position $\alpha_{2000} = 16^h32^m29\overset{s}{.}47$, $\delta_{2000} = -24°28'52\overset{''}{.}6$.

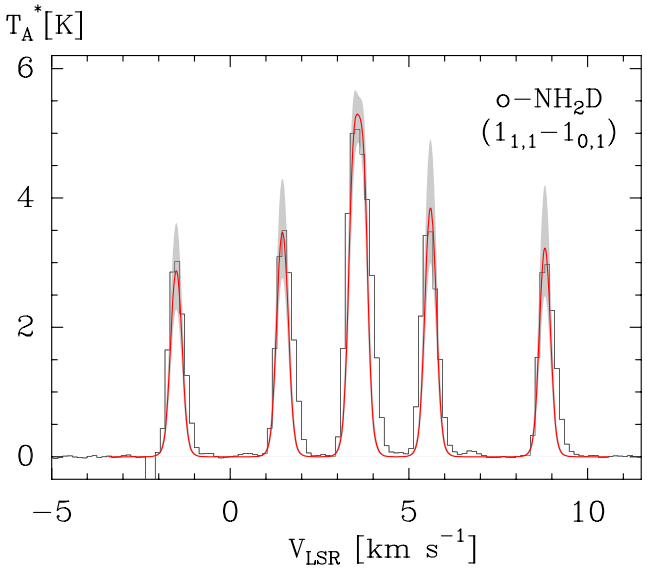

Figure 14. Comparison between model (red curves) and observations (histograms) for the o–NH_2D line observed towards 16293E at the reference position.

The o–NH_2D column density is $\log(N) = 14.54^{+0.13}_{-0.08}$ and with a 3:1 ratio between the ortho and para species, this gives a total column density of $\log(N) = 14.66^{+0.13}_{-0.08}$.

6.2.3 ND_3

As for NH_2D, we model the ND_3 transition by applying an overall scaling factor to the o–NHD_2 abundance profile. The m–ND_3 column density is $\log(N) = 12.27^{+0.15}_{-0.16}$ and with a 16:10:1 ratio between the ortho, meta and para species, this gives a total column density

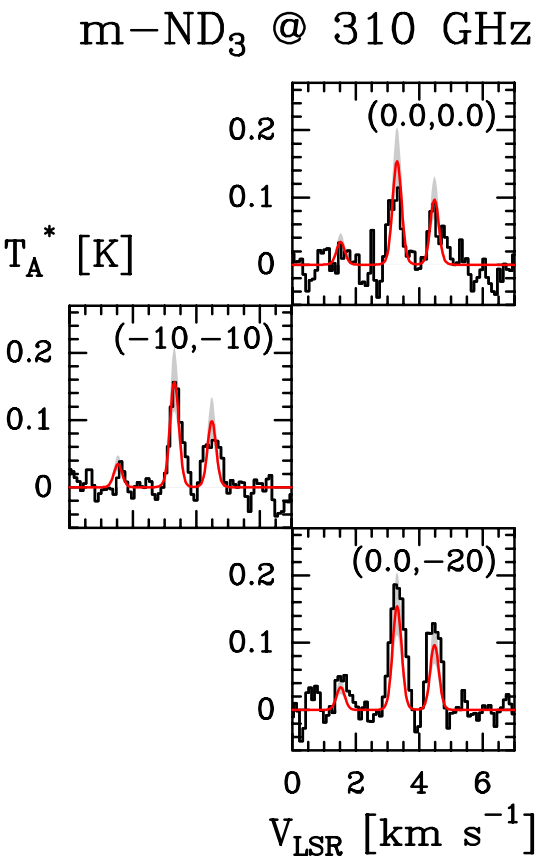

Figure 15. Comparison between model (red curves) and observations (histograms) for the m–ND_3 line observed towards 16293E. The offsets are indicated according to the reference position $\alpha_{2000} = 16^h32^m29\overset{s}{.}47$, $\delta_{2000} = -24°28'52\overset{''}{.}6$.

of $\log(N) = 12.70^{+0.15}_{-0.16}$. The comparison between the model and observations is shown in Fig. 15.

6.2.4 *Discussion*

The column densities derived for the four ammonia isotopologues in 16293E are reported in the second entry of Table 4. Again, our new analysis does not change much the fractionation ratios with respect to the study by Roueff et al. (2005). We thus obtain for 16293E the ratios $NHD_2/NH_2D \sim 0.21$ and $ND_3/NHD_2 \sim 0.05$, which are in fact very similar to those derived in B1b. Such small variations in the fractionation ratios suggest similar physical conditions in both sources and, therefore, similar chemical pathways. We note that these fractionation ratios can be reproduced within a factor of 3 by the gas-phase model of Roueff et al. (2005), but also by a purely statistical grain surface model. Once again, more observations are required to make further progress in our understanding of the deuterium fractionation of ammonia and to rule out one of the two possible scenario.

7 CONCLUSIONS

We used the state-of-the-art PES that describes the NH_3–H_2 interaction (Maret et al. 2009) in order to determine collisional rate coefficients for the ND_2H and ND_3 isotopologues. We subsequently used the Close-Coupling method to calculate a set of collisional rate coefficients for ND_2H, which applies to both the para and ortho symmetries of this molecule. For ND_3, we made specific calculations for the ortho and para species. A few test calculations showed that this latter set was also suitable to treat the meta symmetry of ND_3.

The ND_2H–H_2 rate coefficients were compared to earlier calculations based on the same PES but using a reduced basis for H_2 (Wiesenfeld et al. 2011). We found that the new set shows differences of up to a factor ∼2.5 with respect to the old data. Moreover, the rates which are the most affected are those of highest magnitude. In the case of ND_3, we compared our calculations with ND_3–He calculations (Machin 2006). As previously found for ND_2H (Wiesenfeld et al. 2011) or NH_2D (Daniel et al. 2014), we find large differences between the H_2 and He rate coefficients with variations of up to two orders of magnitude.

Finally, we used these new rate coefficients, as well as the NH_2D–H_2 calculations published earlier (Daniel et al. 2014), in order to re-interpret the observations available in the literature of the various deuterated isotopologues of NH_3 (Roueff et al. 2000, 2005; Lis et al. 2002b, 2006; Gerin et al. 2006). We focused on the B1b and 16293E pre-stellar cores and we used a comprehensive radiative transfer analysis based on the latest estimates of the physical structure of these objects (Daniel et al. 2013; Bacmann et al. 2015). By comparison with the earlier estimates of the column densities, based on approximate methods which did not solve the coupled set of radiative transfer and statistical equilibrium equations, we obtained a modest revision of the column densities. Additionally, the column density ratios of the various deuterated isotopologues agree, within a factor of ∼2–3, with the previous values published for these two objects. This shows that the LTE method, which is often used to carry out a first-order analysis independent of collisional rates, is a reliable alternative to analyse the emission of the NH_3 deuterated isotopologues, at least if one is concerned with obtaining the order of magnitude of the deuterium enrichment. However, in the case a factor of 2 accuracy is required, as when constraints are to be set on the abundance ratios of molecular spin isomers, the new rate coefficients have to be used in a model where the molecular excitation is solved.

ACKNOWLEDGEMENTS

All (or most of) the computations presented in this paper were performed using the CIMENT infrastructure (https://ciment.ujf-grenoble.fr), which is supported by the Rhône-Alpes region (GRANT CPER07_13 CIRA: http://www.ci-ra.org). DL support for this work was provided by NASA (*Herschel* OT funding) through an award issued by JPL/Caltech. This work has been supported by the Agence Nationale de la Recherche (ANR-HYDRIDES), contract ANR-12-BS05-0011-01 and by the CNRS national program 'Physico-Chimie du Milieu Interstellaire'. The authors thanks Q. Ma, P. Dadgigian and A. Van der Avoird for providing some ND_3 cross-sections. We also thank J. Harju for constructive discussions.

REFERENCES

Atkins P. F. R., 2010, Molecular Quantum Mechanics. Oxford Univ. Press, Oxford

Bacmann A. et al., 2015, preprint (arXiv:1512.02629)

Bunker P. R. J. P., 2005, Fundamentals of Molecular Symmetry. Institute of Physics, Bristol

Castets A., Ceccarelli C., Loinard L., Caux E., Lefloch B., 2001, A&A, 375, 40
Coudert L. H., Roueff E., 2006, A&A, 449, 855
Coudert L. H., Roueff E., 2009, A&A, 499, 347
Coudert L., Valentin A., Henry L., 1986, J. Mol. Spectrosc., 120, 185
Daniel F., Cernicharo J., 2008, A&A, 488, 1237
Daniel F., Dubernet M.-L., Meuwly M., 2004, J. Chem. Phys., 121, 4540
Daniel F., Dubernet M.-L., Meuwly M., Cernicharo J., Pagani L., 2005, MNRAS, 363, 1083
Daniel F. et al., 2013, A&A, 560, A3
Daniel F., Faure A., Wiesenfeld L., Roueff E., Lis D. C., Hily-Blant P., 2014, MNRAS, 444, 2544
de Graauw T. et al., 2010, A&A, 518, L6
Dislaire V., Hily-Blant P., Faure A., Maret S., Bacmann A., Pineau Des Forêts G., 2012, A&A, 537, A20
Dubernet M.-L. et al., 2013, A&A, 553, A50
Faure A., Lique F., 2012, MNRAS, 425, 740
Faure A., Hily-Blant P., Le Gal R., Rist C., Pineau des Forêts G., 2013, ApJ, 770, L2
Fusina L., Murzin S., 1994, J. Mol. Spectrosc., 167, 464
Fusina L., Lonardo G. D., Johns J., 1986, J. Mol. Spectrosc., 118, 397
Gerin M., Lis D. C., Philipp S., Güsten R., Roueff E., Reveret V., 2006, A&A, 454, L63
Gerin M., Pety J., Fuente A., Cernicharo J., Commerçon B., Marcelino N., 2015, A&A, 577, L2
Gerlich D., 1993, J. Chem. Soc. Faraday Trans., 89, 2199
Green S., 1976, J. Chem. Phys., 64, 3463
Hermsen W., Wilson T. L., Walmsley C. M., Henkel C., 1988, A&A, 201, 285
Hirano N., Liu F.-C., 2014, ApJ, 789, 50
Hirano N., Kamazaki T., Mikami H., Ohashi N., Umemoto T., 1999, in Nakamoto T., ed., Proc. Star Formation 1999, Nobeyama Radio Observatory, p. 181
Hugo E., 2009, Thesis, Université Pierre et Marie Curie
Jörgensen J. K. et al., 2006, ApJ, 645, 1246
Kalugina Y., Lique F., 2015, MNRAS, 446, L21
Lis D. C., Gerin M., Phillips T. G., Motte F., 2002a, ApJ, 569, 322
Lis D. C., Roueff E., Gerin M., Phillips T. G., Coudert L. H., van der Tak F. F. S., Schilke P., 2002b, ApJ, 571, L55
Lis D. C., Gerin M., Roueff E., Vastel C., Phillips T. G., 2006, ApJ, 636, 916
Lucia F. C. D., Helminger P., 1975, J. Mol. Spectrosc., 54, 200
Ma Q., van der Avoird A., Loreau J., Alexander M. H., van de Meerakker S. Y. T., Dagdigian P. J., 2015, J. Chem. Phys., 143, 044312
Machin L., 2006, Thesis, Université Pierre et Marie Curie
Machin L., Roueff E., 2007, A&A, 465, 647
Maret S., Faure A., Scifoni E., Wiesenfeld L., 2009, MNRAS, 399, 425
Marquette J. B., Rebrion C., Rowe B. R., 1988, J. Chem. Phys., 89, 2041
Maue A.-W., 1937, Ann. Phys., Lpz., 422, 555
Menten K. M. et al., 2010, A&A, 521, L7
Offer A., Flower D. R., 1989, J. Phys. B: At., Mol. Opt. Phys., 22, L439
Persson C. M. et al., 2012, A&A, 543, A145
Persson C. M. et al., 2015, preprint (arXiv:1511.05486)
Pilbratt G. L. et al., 2010, A&A, 518, L1
Rist C., Faure A., 2011, J. Math. Chem., 50, 588
Rist C., Alexander M. H., Valiron P., 1993, J. Chem. Phys., 98, 4662
Rist C., Faure A., Hily-Blant P., Le Gal R., 2013, J. Phys. Chem. A, 117, 9800
Roberts H., Herbst E., Millar T. J., 2003, ApJ, 591, L41
Roueff E., Tiné S., Coudert L. H., Pineau des Forêts G., Falgarone E., Gerin M., 2000, A&A, 354, L63
Roueff E., Lis D. C., van der Tak F. F. S., Gerin M., Goldsmith P. F., 2005, A&A, 438, 585
Roueff E., Loison J. C., Hickson K. M., 2015, A&A, 576, A99
Saito S., Ozeki H., Ohishi M., Yamamoto S., 2000, ApJ, 535, 227
Schöier F. L., van der Tak F. F. S., van Dishoeck E. F., Black J. H., 2005, A&A, 432, 369
Scribano Y., Faure A., Wiesenfeld L., 2010, J. Chem. Phys., 133, 231105
Shah R. Y., Wootten A., 2001, ApJ, 554, 933
Sipilä O., Caselli P., Harju J., 2015, A&A, 578, A55
Sunderlin L. S., Armentrout P. B., 1994, J. Chem. Phys., 100, 5639
Tiné S., Roueff E., Falgarone E., Gerin M., Pineau des Forêts G., 2000, A&A, 356, 1039
Tkáč O., Orr-Ewing A. J., Dagdigian P. J., Alexander M. H., Onvlee J., van der Avoird A., 2014, J. Chem. Phys., 140,
Tkáč O., Saha A. K., Loreau J., Ma Q., Dagdigian P. J., Parker D. H., van der Avoird A., Orr-Ewing A. J., 2015, Mol. Phys., 1
Townes C. H. S. A., 2012, Microwave Spectroscopy. Dover Press, New York
van der Tak F. F. S., Schilke P., Müller H. S. P., Lis D. C., Phillips T. G., Gerin M., Roueff E., 2002, A&A, 388, L53
W. Gordy R. L. C., 1984, Microwave Molecular Spectra. Wiley Interscience, New York
Wiesenfeld L., Scifoni E., Faure A., Roueff E., 2011, MNRAS, 413, 509
Yang B. H., Stancil P. C., 2008, Eur. Phys. J. D, 47, 351

APPENDIX A: ND_3 ROTATIONAL LEVELS

ND_3 rotational levels can be inferred from ammonia spectroscopy (Townes 2012). In their ground electronic state, both NH_3 and ND_3 are symmetric top with a C_{3v} pyramidal symmetry. The symmetric top rotational levels are labelled J_K where J stands for the rotational momentum quantum number and K is its absolute projection along the symmetry axis. The rotation states are eigenstates of the symmetric top Hamiltonian, namely $|JKm\rangle$ where m is the projection quantum number of the angular momentum along any space-fixed axis (Green 1976). All rotational levels J_K are degenerate in m.

As for ammonia, the nitrogen atom can tunnel back and forth through the deuterium plane. In this umbrella vibrational mode (ν_2) the potential presents a double minimum along the inversion coordinate. This results in the splitting of all rotational levels into two inversion levels (states), respectively, symmetric $|+\rangle$ and antisymmetric $|-\rangle$ with respect to the inversion coordinate. Although we neglect any vibrational coupling during the collision, the weak energy splitting between inversion levels is set to a constant 0.053 cm^{-1} (Fusina, Lonardo & Johns 1986; Fusina & Murzin 1994; Tkáč et al. 2014) independantly of the rotational level. The lower inversion level $|+\rangle$ is symmetric whereas the upper level $|-\rangle$ is antisymmetric with respect to the inversion coordinate.

A1 Deuterium permutation symmetry

Because D nuclei have a nuclear–spin I = 1, they obey Bose–Einstein statistics and the total internal wavefunction of ND_3 is unchanged by permutation of two identical D. Thus, the determination of all allowed internal states requires the description of the deuterium nuclear–spin states together with the symmetry under permutation of the three identical D atoms for both motional and nuclear–spin states. From Bose–Einstein statistics one derives new statistical weights of the rotation–inversion levels compared to NH_3 (Bunker 2005; Hugo 2009).

In the ground electronic state, the molecular symmetry group of ND_3 is C_{3v} and the complete nuclear–spin permutation group is S_3 (Bunker 2005). The associated irreducible representations correspond to A_1, A_2 and E symmetry species. The one dimension symmetry adapted basis of A_1 and A_2 symmetry are wavefunctions, respectively, symmetric and antisymmetric under permutation of

two nuclei whereas in any two dimension basis that spans the E representation, the permutation matrix is non-diagonal. In the following we recall the symmetry species of each rotational, inversion and nuclear–spin state.

A2 Permutation symmetry adapted motional states

As for ammonia, the symmetric top rotational states transform as follows under permutation $\mathcal{P}$ of two deuterons (Bunker 2005; Townes 2012):

$$\mathcal{P}\,|JKm\rangle = (-1)^J e^{-2in\pi K/3}\,|J\,-\,Km\rangle\,; n = 1, 2, 3.$$

Thus, symmetry adapted rotational states are combinations of $|JKm\rangle$ and $|J\,-\,Km\rangle$ states (Townes 2012). Symmetric and antisymmetric combinations of $|JKm\rangle$ and $|J\,-\,Km\rangle$, for which K is a multiple of 3, span the A_1 and A_2 representations:

$$|JKm\,\alpha\rangle = \sqrt{\frac{1}{2(1+\delta_{K0})}}(|JKm\rangle + \alpha\,|J\,-\,Km\rangle); \alpha = \pm 1$$

$$\mathcal{P}\,|JKm\,\alpha\rangle = \alpha(-1)^J\,|JKm\,\alpha\rangle\,.$$

For each rotational level J_K the permutation symmetry species A_1 or A_2 are given by the sign of $\alpha(-1)^J$. Rotational states of both symmetries exist with the exception of $K = 0$ for which $\alpha = 1$ and even J states span the A_1 symmetry whereas odd J states span the A_2 symmetry. Any basis ($|JKm\rangle$; $|J\,-\,Km\rangle$) of rotational states for which K is not a multiple of 3 spans a representation of E symmetry.

For the inversion motion the symmetric and antisymmetric vibrational states $|+\rangle$ and $|-\rangle$ span, respectively, the A_1 and A_2 symmetry (Townes 2012):

$$\mathcal{P}\,|\pm\rangle = \pm\,|\pm\rangle\,.$$

A3 Symmetry adapted nuclear–spin states

The total nuclear–spin wavefunction is obtained from the coupling of three deuterium nuclear–spin momentum with nuclear–spin quantum number $I = 1$. The direct product of the three deuteron nuclear–spin states (with $m_I = -1, 0, 1$) where m_I is the nuclear–spin projection quantum number, gives $3^3 = 27$ deuterium spin states for ND_3. In terms of nuclear–spin angular momentum, from the single deuteron rotation group irreducible representation, D_1 one builds the complete nuclear–spin representation as the direct product: $(D_1)^3$ which decomposes as follows on the total nuclear–spin irreducible representations D_I of total quantum number I (Atkins 2010):

$$D_1^3 = D_3 + 2D_2 + 3D_1 + D_0.$$

Each of the angular momentum basis characterized by (I, m_I) spans the permutation symmetry species $\Gamma_{ns,\,I}$ as follows (Machin 2006; Hugo 2009): $I = 3 \rightarrow A_1$, $I = 2 \rightarrow E$, $I = 1 \rightarrow A_1 + E$ and $I = 0 \rightarrow A_2$. Thus, the angular momentum representation characterized by the total nuclear–spin I generate the permutation symmetry representations $\Gamma_{ns,\,I}$ (Hugo 2009):

$$D_3 = 7A_1 \tag{A1}$$

$$2D_2 = 5E \tag{A2}$$

$$3D_1 = 3A_1 + 3E \tag{A3}$$

$$D_0 = A_2. \tag{A4}$$

Table A1. Direct product representation of S_3.

$\Gamma\otimes\Gamma'$	A_1	A_2	E
A_1	A_1	A_2	E
A_2	A_2	A_1	E
E	E	E	A_1+A_2+E

In terms of permutation group, the total nuclear–spin representation Γ_{tot} decomposes on the irreducible representations $\Gamma_{ns} = A_1, E, A_2$ as follows:

$$\Gamma_{tot} = \sum\nolimits_{I,\Gamma_{ns,I}} (2I+1)\Gamma_{ns,I} = 10A_1 + 8E + A_2.$$

For the total nuclear–spin basis (of 27 nuclear–spin states), the symmetry degeneracies are, respectively, ($g_{A_1} = 10$, $g_E = 16$, $g_{A_2} = 1$). We note that the E representation is of dimension 2 and therefore the number of nuclear–spin basis states of E symmetry is 16. From this decomposition we identify the three ND_3 nuclear–spin modifications as defined by Maue (1937), in decreasing order of the symmetry degeneracy g_{ns}: ortho (E, $g_{ns} = 16$), meta (A_1, $g_{ns} = 10$) and para (A_2, $g_{ns} = 1$).

A4 Nuclear–spin statistics

The total nuclear–spin rotation inversion wavefunctions are obtained from the direct product of nuclear–spin states with the rotation states and vibration state. The direct product of two S_3 irreducible representations generates a new representation shown in Table A1 (Bunker 2005; Atkins 2010).

Because of Bose–Einstein principle the complete wavefunction is unchanged by the interchange of two deuterium. In terms of permutation symmetry it belongs to the A_1 symmetry of S_3. Therefore, given the symmetry species A_1 and A_2 of ND_3 inversion states $|+\rangle$ and $|-\rangle$, each inversion state can only combine to nuclear–spin–rotation states of the same symmetry. The symmetry species of the nuclear–spin–rotation states can also be deduced from the direct product of Table A1. The para and meta nuclear–spin state of symmetry A_2 or A_1 can combine to any A symmetry rotational state with $K = 3n$, whereas the ortho nuclear–spin states of symmetry E can combine to any E symmetry rotational state with $K \neq 3n$. The symmetry of the resultant direct product nuclear–spin–rotation state is either A_1 or A_2.

In reference to previous description of ammonia (Green 1976; Offer & Flower 1989; Rist, Alexander & Valiron 1993; Ma et al. 2015), for each modification, the symmetry adapted ND_3 nuclear–spin–rotation–inversion states are commonly labelled by $|JKm\epsilon\rangle\,|\pm\rangle$ where $\epsilon = \pm 1$ specifies the symmetry of the nuclear–spin–rotation state: $\mathcal{P}\,|JKm\epsilon\rangle = \epsilon(-1)^J\,|JKm\epsilon\rangle$ for the meta and ortho modifications and $\mathcal{P}\,|JKm\epsilon\rangle = -\epsilon(-1)^J\,|JKm\epsilon\rangle$ for the para modification. Therefore each nuclear–spin–rotation–inversion state is uniquely defined by the label $|JKm\epsilon\rangle\,|\pm\rangle$. Conversely, for a given spin isomer, it is only necessary to specify either ϵ or the inversion state since these quantities are related through the relations: $\epsilon = -(-1)^J\,|\pm\rangle$ for p–ND_3 and $\epsilon = (-1)^J\,|\pm\rangle$ for o–ND_3 or m–ND_3. We note that this definition of ϵ is consistent with the previous description of NH_3 spin–rotation states but leads to an opposite inversion symmetry for the meta and ortho modifications (Ma et al. 2015).

For rotational states with $K = 0$, as the spin–rotation states $|J0m\epsilon\rangle$ are restricted to $\epsilon = 1$ only one of the inversion state

Table A2. Permutation symmetry of ND_3 nuclear–spin–rotation–inversion states: $|J\,K\,m\epsilon\rangle\,|\pm\rangle$.

Nuclear–spin (Γ_{ns})	Γ_{rot}	$\Gamma_{ns}\otimes\Gamma_{rot}$	Γ_{inv}	K	$J_{K=0}$	ϵ	$\|\pm\rangle$	g_{ns}
Para (A_2)	A_2	A_1	A_1	$3n$	J odd	$-(-1)^J$	$\|+\rangle$	1
	A_1	A_2	A_2	$3n$	J even	$(-1)^J$	$\|-\rangle$	1
Meta (A_1)	A_1	A_1	A_1	$3n$	J even	$(-1)^J$	$\|+\rangle$	10
	A_2	A_2	A_2	$3n$	J odd	$-(-1)^J$	$\|-\rangle$	10
Ortho (E)	E	A_1	A_1	$3n\pm1$	–	$(-1)^J$	$\|+\rangle$	8
	E	A_2	A_2	$3n\pm1$	–	$-(-1)^J$	$\|-\rangle$	8

Table A3. Nuclear–spin statistics of rotation–inversion states for ND_3.

K	J	ϵ	$\|\pm\rangle$	Spin modification	g_{ns}
0	even	1	$\|+\rangle$	Meta	10
	even	1	$\|-\rangle$	Para	1
	odd	1	$\|+\rangle$	Para	1
	odd	1	$\|-\rangle$	Meta	10
$3n\neq0$	all	$(-1)^J$	$\|+\rangle$	Meta	10
	all	$-(-1)^J$	$\|+\rangle$	Para	1
	all	$-(-1)^J$	$\|-\rangle$	Meta	10
	all	$(-1)^J$	$\|-\rangle$	Para	1
$3n\pm1$	all	$(-1)^J$	$\|+\rangle$	Ortho	8
	all	$-(-1)^J$	$\|-\rangle$	Ortho	8

$|\pm\rangle$ fulfills Bose–Einstein principle; $\pm(-1)^J=1$ for the A_1 meta spin states and $\pm(-1)^J=-1$ for the A_2 para spin states. For all other rotational states with $K\neq0$, both inversion states can combine to the rotation–nuclear–spin states. A summary of the permutation symmetry of all nuclear–spin–rotation–inversion states with their nuclear–spin weights is given in Table A2. The spin statistics of all rotation–inversion states is deduced in Table A3. The consequent rotational energy level diagram is given by Tkáč et al. (2014).

This paper has been typeset from a TEX/LATEX file prepared by the author.